Journal of Catalysis 454 (2026) 116641

Contents lists available at ScienceDirect

Journal of Catalysis

journal homepage: www.elsevier.com/locate/jcat

Revisiting the activity of Ru-hcp(001) and Ru-fcc(111) for alkaline HER: A DFT study

Lea Gašparič, Anton Kokalj *

Department of Physical and Organic Chemistry, Jožef Stefan Institute, Jamova 39, SI 1000, Ljubljana, Slovenia
Jožef Stefan International Postgraduate School, Jamova 39, SI 1000, Ljubljana, Slovenia

ARTICLE INFO

Keywords:
DFT calculations
Ruthenium
Water dissociation
Hydrogen evolution reaction (HER)

ABSTRACT

We present a comprehensive density-functional-theory (DFT) study of the water dissociation reaction on Ru-hcp(001) and Ru-fcc(111). The motivation stems from experiments showing that supported fcc-structured Ru nanoparticles outperform hcp-structured ones as catalysts for the hydrogen evolution reaction (HER) in alkaline media, as well as from prior combined experimental and computational work (Zheng et al., 2016) attributing this difference to intrinsic activity of the two facets derived from DFT calculations. By systematically varying slab thickness, supercell size, and water models, and by rigorously evaluating vibrational contributions to the Gibbs energy, we demonstrate that reaction Gibbs energies strongly depend on model details, whereas activation Gibbs energies are less sensitive. Importantly, when vibrational contributions are treated rigorously, water dissociation is predicted to exhibit slightly lower activation Gibbs energy on Ru-hcp(001), suggesting that it should be somewhat more active than Ru-fcc(111). This finding contrasts with the earlier aforementioned study, whose reported data reveal that Ru-fcc(111) is more active due to favorable vibrational contributions. This discrepancy stems primarily from the incomplete treatment of vibrational contributions in the earlier work and from the omission of corrections for low-frequency modes. Our results highlight the need to consider additional factors – such as support effects and the relative abundance and intrinsic activity of different facets present on Ru nanoparticles – to explain the experimentally observed superior alkaline HER activity of fcc-structured Ru nanoparticles. They further underscore the critical role of accurately evaluating vibrational Gibbs energy contributions in computational heterogeneous catalysis.

1. Introduction

Hydrogen is a promising alternative to carbon-based fuels, and water electrolysis stands out as one of the most viable green methods for its production. This process involves two half-reactions: the hydrogen evolution reaction (HER) and the oxygen evolution reaction (OER).

Platinum (Pt) is the benchmark catalyst for HER under acidic conditions due to its exceptional activity, but its high cost motivates the search for cheaper alternatives. In the quest for more affordable materials, ruthenium (Ru) has emerged as a promising HER catalyst under alkaline conditions, due to its lower cost and good catalytic performance [1–4].

In alkaline media, the kinetics of HER are 2–3 orders of magnitude slower than expected [5,6]. Several explanations have been proposed to account for this unexpected behavior [5–7], including the identity of the proton donor, the influence of co-adsorbed species, and solvent reorganization effects. Unlike acidic conditions, where protons are readily available from hydronium ions (H_3O^+), alkaline HER must rely on water molecules as the proton source. As a result, the Volmer step – generally considered the rate-limiting step under alkaline conditions – can be written as:

$$H_2O + e^- \longrightarrow H^* + OH^-, \quad (1)$$

where H* denotes a chemisorbed hydrogen atom on the catalyst surface.

Compared to Pt, Ru exhibits superior water-splitting performance under alkaline conditions [4], further highlighting its potential as a cost-effective HER catalyst. One promising strategy for improving the catalytic activity of Ru involves tailoring its crystal structure [2,4]. While bulk Ru naturally crystallizes in the hexagonal close-packed (hcp) structure, Kusada et al. [8] successfully synthesized and characterized face-centered cubic (fcc) Ru nanoparticles in 2013. Their study demonstrated that the catalytic activity of Ru nanoparticles for CO oxidation depends on both crystal structure and particle size, with the fcc

* Corresponding author at: Department of Physical and Organic Chemistry, Jožef Stefan Institute, Jamova 39, SI 1000, Ljubljana, Slovenia.
E-mail address: tone.kokalj@ijs.si (A. Kokalj).
URL: http://www.ijs.si/ijsw/K3-en/Kokalj (A. Kokalj).

https://doi.org/10.1016/j.jcat.2025.116641
Received 17 October 2025; Received in revised form 7 December 2025; Accepted 14 December 2025
Available online 19 December 2025

structure showing higher activity for particles larger than 3 nm. Since then, the uncommon fcc phase has been reported in a variety of applications [9–13], including HER [14–17]. For example, Zheng et al. [14] synthesized a highly active Ru catalyst supported on C_3N_4/C containing the fcc phase, while Li et al. [16] reported enhanced HER performance for a MoO_x/Ru-fcc catalyst compared to its hcp counterpart.

While experimental evidence suggests that Ru-fcc catalysts exhibit higher activity than their Ru-hcp counterparts, the mechanistic origin of this difference remains insufficiently understood. Several density-functional theory (DFT) studies have attempted to address this issue, but the findings are conflicting. For instance, Li et al. [18] calculated hydrogen adsorption energies on various Ru surfaces and concluded that Ru-fcc(111) is less active, implying that the hcp phase may offer superior HER performance. In contrast, Chen et al. [15] studied a RuNi system interacting with a single water molecule and reported a lower activation barrier for water dissociation on the fcc phase. A highly influential study by Zheng et al. [14], employing an ice-like water bilayer model, also reported lower activation barrier for water dissociation on Ru-fcc(111) compared to Ru-hcp(001). However, their results are based on thin slab models and omit corrections for low-frequency vibrational modes, which appear to be the dominant factor favoring the fcc phase in their calculations, as discussed in the Results and discussion section. These methodological deficiencies raise concerns about the validity of their results.

This study aims to resolve the inconsistencies reported in the literature by providing a comprehensive computational analysis of the catalytic activity of ideal Ru-hcp(001) and Ru-fcc(111) surfaces toward HER. It is important to emphasize that due to the exponential dependence of reaction rates on activation energies, even small differences in calculated activation barriers can lead to significant variations in predicted activity. In our DFT calculations, we observed that the activity of Ru-fcc(111) and Ru-hcp(001) surfaces is particularly sensitive to computational parameters, such as slab thickness. As a result, using non-converged or insufficiently tested models can easily lead to misleading conclusions.

2. Technical details

DFT calculations were performed using the Quantum ESPRESSO software package [19,20], employing the Perdew–Burke–Ernzerhof (PBE) exchange–correlation functional [21]. A plane-wave basis set in combination with projector-augmented wave (PAW) pseudopotentials from the PSLibrary was used [22–24]. The kinetic energy cutoff was set to 50 Ry for the wavefunctions and 575 Ry for the charge density. Brillouin-zone integrations were performed using the special-point technique [25] with a Methfessel–Paxton smearing [26] of 20 mRy. All structures were relaxed until force components were below 1×10^{-3} Ry/bohr.

Grimme-D3 dispersion correction with two-body terms only was applied to account for van der Waals interactions [27]. The three-body terms were omitted in order to allow vibrational frequency calculations using the `ph.x` module of Quantum ESPRESSO, which does not support them. We verified that the omission of three-body terms has a negligible effect on adsorption and activation energies (see Tables S1–S3 in the Supplementary material) and does not alter the qualitative conclusions of this study.

Ru-hcp(001) and Ru-fcc(111) slabs were constructed using the optimized bulk lattice parameters, with slab thicknesses ranging from 3 to 8 atomic layers. For the hcp phase, the optimized lattice constants are $a = 2.719$ Å and $c = 4.288$ Å, while for the fcc phase, the lattice constant is $a = 3.811$ Å. The in-plane Ru–Ru bond length in the fcc phase (2.695 Å) is slightly shorter than in the hcp phase (2.719 Å). In all cases, adsorbates were placed only on the top side of the slab, the bottom layer atoms were fixed at their bulk positions, and a vacuum region of 20 Å was added above the slab, along with a dipole correction [28]. For thicker slabs, convergence tests were also carried out by relaxing only the three topmost layers. Both approaches yielded consistent results, as evidenced in the Results and discussion section.

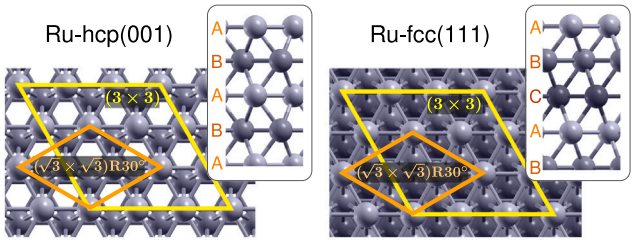

Fig. 1. Ru-hcp(001) and Ru-fcc(111) surfaces with the $(\sqrt{3} \times \sqrt{3})$R30° and (3×3) supercells indicated in orange and yellow, respectively. Side views show the stacking sequences of layers. (For interpretation of the references to color in this figure legend, the reader is referred to the web version of this article.)

Calculations were primarily performed using two supercells: a smaller $(\sqrt{3} \times \sqrt{3})$R30° supercell containing 3 Ru atoms per layer, and a larger (3×3) supercell containing 9 atoms per layer. Additionally, a few convergence tests were carried out using larger (4×4) and (6×6) supercells. The Brillouin zone was sampled using a $7 \times 7 \times 1$ k-point mesh for the $(\sqrt{3}\times\sqrt{3})$R30° supercell and a $4 \times 4 \times 1$ mesh for the (3×3) one; the (4×4) and (6×6) supercells were sampled using $3 \times 3 \times 1$ and 2×2×1 k-point meshes, respectively. The geometries of the Ru-hcp(001) and Ru-fcc(111) surfaces, along with their corresponding supercells, are shown in Fig. 1. The primary structural difference between the two surfaces lies in their stacking sequence: Ru-hcp(001) follows an ABABAB stacking, while Ru-fcc(111) exhibits an ABCABC pattern.

To model water dissociation, two different representations of water were employed: a single H_2O molecule and an ice-like water bilayer positioned above the Ru surface [29]. The utilized bilayer model consists of two distinct types of water molecules: one oriented with a hydrogen atom pointing toward the surface, and another adsorbed via the oxygen atom, with both hydrogen atoms aligned parallel to the surface. For the single water-molecule model, in addition to the *in vacuo* calculations, we also performed calculations with an implicit aqueous solvent using the self-consistent continuum-solvation model as implemented in the Environ plugin [30] of Quantum ESPRESSO. Due to convergence problems in the structural relaxations with the implicit solvent, only single-point SCF calculations were carried out on the geometries optimized in vacuum.

Transition states (TS) for water dissociation were identified using the climbing-image nudged elastic band (CI-NEB) method [31,32]. For frequency calculations, the TS geometries obtained from the CI-NEB calculations were further refined using the ARTn plugin [33,34] for Quantum ESPRESSO, until the forces on all atoms were below 7×10^{-4} Ry/bohr.

Vibrational contributions to Gibbs energies were calculated at 25 °C. To this end, structures were re-optimized by relaxing all degrees of freedom, including the bottom atomic layer. Phonon calculations were performed at the Γ q-point. For the smaller $(\sqrt{3}\times\sqrt{3})$R30° supercell, all atoms were perturbed, and the acoustic sum rule was applied to enforce three translational zero-frequency modes. In contrast, for the larger (3×3) supercell, only the atoms of the water bilayer were perturbed to reduce the computational cost. Vibrational contributions to the Gibbs energy were estimated using the quasi-harmonic approximation of Cramer–Truhlar [35], in which all vibrational frequencies below 100 cm^{-1} are raised to 100 cm^{-1} to account for the breakdown of the harmonic oscillator model for low-frequency modes (at room temperature, 100 cm^{-1} corresponds to about $k_BT/2$, where k_B is the Boltzmann constant).[1] The vibrational contributions were computed using an in-house adaptation [36] of the `dynmat.x` utility from Quantum

[1] Vibrational modes with frequencies below $k_BT/2$ behave more like hindered rotations than true vibrations. A hindered-rotor mode contributes on the order of $k_BT/2$ to the thermal energy, providing a physical motivation for the commonly used 100 cm^{-1} cutoff in the Cramer–Truhlar correction

ESPRESSO. The nature of the adsorption bonding was analyzed using the integrated local density of states (ILDOS), the projected density of states (PDOS), crystal orbital Hamilton populations (COHP), and COHP integrated up to the Fermi energy (ICOHP). PDOS, COHP, and ICOHP were computed with the LOBSTER code [37].

Molecular graphics were produced using the XCrySDen graphical package [38], graphs were plotted with the Gnuplot software [39], and image post-processing was performed in Inkscape [40].

2.1. Energy equations

Adsorption binding energies of H* and OH* were calculated according to the following equation:

$$E_b = E_{X/slab} - E_{slab} - E_X, \tag{2}$$

where $E_{X/slab}$ is the total energy of the Ru slab with the adsorbed species (X = H, OH), E_{slab} is the energy of the bare Ru slab, and E_X is the energy of the isolated H or OH radical; OH was treated with spin polarization, whereas for H, a reference energy of 1 Ry was used.

Reaction energy (ΔE) and activation energies (E^{act}) were calculated as:

$$\Delta E = E_{FS} - E_{IS} \tag{3}$$

and

$$E^{act} = E_{TS} - E_{IS}, \tag{4}$$

where E_{IS}, E_{TS}, and E_{FS} denote the total energies of the initial state (IS), transition state (TS), and final state (FS), respectively.

The E terms in Eqs. (2)–(4) represent Kohn–Sham total energies calculated at 0 K without the zero-point energy (ZPE). In addition to these 0 K energies, Gibbs energies at room temperature were also calculated.

For bare surfaces and surfaces with adsorbates, only vibrational contributions to thermal energy and entropy were considered, whereas the configurational entropy of adsorbates was neglected. The pV term was also omitted, as it is negligible for solids at ambient pressure. Consequently, the Gibbs energy is expressed as:

$$G(T) = E_0 + E_{vib}(T) - T S_{vib}(T), \tag{5}$$

where E_0 is the Kohn–Sham total energy at 0 K, excluding ZPE. The subscript 0 is used here explicitly to denote zero temperature, whereas it was omitted in Eqs. (2)–(4) for brevity. $E_{vib}(T)$ denotes the vibrational thermal energy at temperature T, including ZPE, and $S_{vib}(T)$ is the vibrational entropy. This notation implies that $E_{vib}(0)$ = ZPE. For convenience, Eq. (5) can be rewritten as:

$$G(T) = E_0 + G_{corr}(T), \tag{6}$$

where $G_{corr}(T)$ represents the vibrational correction that must be added to E_0 to obtain the Gibbs energy $G(T)$. In contrast, for gaseous species, roto-translational contributions were also taken into account (cf. Eq. (S7) in the Supplementary material).

Reaction and activation Gibbs energies (ΔG and G^{act}) were calculated analogously to Eqs. (3) and (4), by replacing the total energies E with the corresponding Gibbs energies $G(T)$. For transition-state structures, the vibrational mode associated with the imaginary frequency – corresponding to the reaction coordinate – was excluded from the vibrational contribution, as prescribed by the transition-state theory.

3. Results and discussion

In this section, we systematically investigate the catalytic activity of Ru-hcp(001) and Ru-fcc(111) toward the water dissociation reaction. The primary goals are to assess the performance of each surface and to resolve the conflicting results reported in the literature, as discussed in the Introduction.

We begin by analyzing the adsorption binding energies of H* and OH*, with a particular focus on their convergence with respect to slab thickness. This is followed by an analysis of reaction and activation energies for the water dissociation step. As is commonly done in conventional DFT studies, the Volmer reaction step (1) is approximated by a dissociation reaction of adsorbed water molecule in which the final state contains a chemisorbed OH* instead of a hydrated hydroxide ion:

$$H_2O^* \longrightarrow H^* + OH^*. \tag{7}$$

It should be noted that, at the reversible hydrogen electrode (RHE) potential, reaction Gibbs energies for the Volmer reaction step (1) can be obtained from reaction (7) by using an appropriate thermodynamic cycle, as described in the Supplementary material (Scheme S1 and Eq. (S6)).

All reaction pathway calculations were performed across multiple slab thicknesses to ensure proper convergence of both reaction and activation energies.

3.1. Adsorption characteristics of H and OH moieties

3.1.1. Convergence of adsorption binding energies

Adsorption binding energies of H and OH were calculated across different coverages and Ru slab thicknesses to assess their convergence. The $(\sqrt{3}\times\sqrt{3})R30°$ and (3×3) supercells were employed to represent high (1/3 ML) and low (1/9 ML) coverages, respectively. Various high-symmetry adsorption sites were examined, as such calculations help rationalize energy trends observed during the water dissociation reaction—particularly because, at the transition state, the H and OH fragments are not yet located over their most favorable binding sites.

Convergence of H and OH adsorption binding energies for the top and fcc sites on Ru-hcp(001) and Ru-fcc(111) with respect to slab thickness is reported in Table 1. The results show that binding energies obtained using 3- and 4-layer slabs are generally not converged. Therefore, the use of thicker slabs is recommended for reliable results.

For slabs thicker than four layers, we also tested relaxing only the topmost three Ru layers while keeping the rest fixed (values in parentheses in Table S1 of the Supplementary material) and found that the effect on the results is minimal. To assess the depth of charge redistribution upon adsorption, planar-integrated electron charge density difference plots are shown in Fig. S2 of the Supplementary material. These plots indicate that charge redistribution is still clearly present at the third atomic layer and progressively vanishes deeper into the slab. This observation supports the conclusion that relaxing three or more layers is sufficient to accurately model adsorption.

Table 2 reports the adsorption binding energies of H and OH on various high-symmetry sites for both supercell sizes, using slabs six atomic layers thick. The H binding energies are very similar between the two supercells, with the fcc site being the most stable on both Ru-hcp(001) and Ru-fcc(111), yielding nearly identical adsorption energies (see also Table 1). The hcp site follows in stability, where Ru-fcc(111) binds H slightly more strongly than Ru-hcp(001). The bridge site is not stable on either surface; therefore, the reported energies for this configuration were obtained from constrained relaxations and show nearly identical values for both crystal phases. The least stable site is the top site, which exhibits a more pronounced difference between the two surfaces: Ru-hcp(001) binds H approximately 0.1 eV more strongly than Ru-fcc(111). Previous studies also identified the fcc site as the most stable adsorption site for H on both surfaces [12,13]; however, those studies report stronger H binding on Ru-fcc(111) than Ru-hcp(001), which is not observed in the present work.

Because the optimized lattice parameters of Ru-fcc and Ru-hcp yield slightly different Ru–Ru nearest-neighbor distances (by 0.02 Å), we examined the effect of this structural difference on adsorption binding energies. Specifically, we modeled H adsorption on the top site using both Ru-fcc and Ru-hcp compatible lattice parameters. The

Table 1
Convergence of adsorption binding energies (in eV) of H and OH at fcc and top sites on Ru-hcp(001) and Ru-fcc(111) with respect to slab thickness. N denotes the number of Ru layers in the slab.

	E_b(H @ fcc)		E_b(H @ top)		E_b(OH @ fcc)		E_b(OH @ top)[a]	
N	Ru-hcp(001)	Ru-fcc(111)	Ru-hcp(001)	Ru-fcc(111)	Ru-hcp(001)	Ru-fcc(111)	Ru-hcp(001)	Ru-fcc(111)
3	−2.89	−2.94	−2.52	−2.35	−3.38	−3.20	−3.10	−2.87
4	−2.97	−2.97	−2.52	−2.48	−3.47	−3.50	−3.10	−3.11
5	−2.96	−2.94	−2.53	−2.40	−3.47	−3.41	−3.11	−3.02
6	−2.95	−2.95	−2.53	−2.42	−3.41	−3.41	−3.12	−3.03
7	−2.96	−2.93	−2.52	−2.42	−3.43	−3.42	−3.12	−3.04
8	−2.96	−2.95	−2.53	−2.40	−3.44	−3.40	−3.12	−3.01

[a] Obtained by laterally constraining the bottommost adsorbate atom.

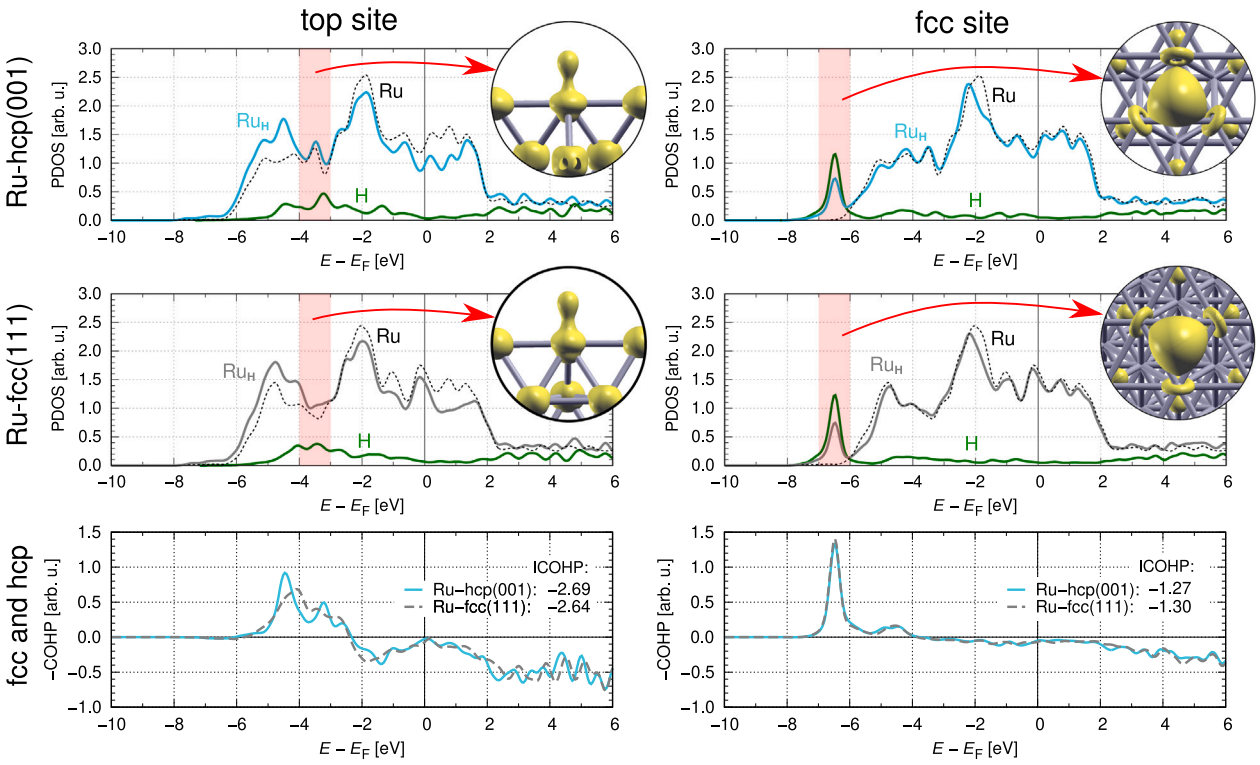

Fig. 2. Projected density of states (PDOS) for the adsorbed H atom and the underlying Ru surface atom (solid curves) on Ru-hcp(001) [top-row panels] and Ru-fcc(111) [middle-row panels], and the crystal orbital Hamilton populations (COHP) for both surfaces [bottom-row panels]. H adsorption at the top site is shown in the left column, while the right column corresponds to the fcc site. The PDOS of the surface Ru atom of a bare surface is shown for comparison with dotted black curves. The integrated local density of states (ILDOS) illustrating the H–Ru interaction is also shown. For the top site, the ILDOS energy range is from −4 to −3 eV, whereas for the fcc site, it is from −7 to −6 eV, as indicated by pale red vertical bands. The integrated COHP (ICOHP) values are also shown on the COHP plots. (For interpretation of the references to color in this figure legend, the reader is referred to the web version of this article.)

Table 2
Adsorption binding energies (in eV) of H and OH at different sites on Ru-hcp(001) and Ru-fcc(111). Results were obtained using six-layer slabs and the $(\sqrt{3}\times\sqrt{3})$R30° and (3×3) supercells.

supercell	E_b(H)		E_b(OH)	
site	Ru-hcp(001)	Ru-fcc(111)	Ru-hcp(001)	Ru-fcc(111)
$(\sqrt{3}\times\sqrt{3})$R30°				
top	−2.53	−2.42	−3.12[a]	−3.03[a]
bridge	−2.79[a]	−2.80[a]	−3.39	−3.39
fcc	−2.95	−2.95	−3.41	−3.41
hcp	−2.85	−2.88	−3.43	−3.32
(3×3)				
top	−2.53	−2.44	−3.13[a]	−3.04[a]
bridge	−2.80[a]	−2.81[a]	−3.42	−3.36[a]
fcc	−2.96	−2.96	−3.46	−3.49
hcp	−2.86	−2.90	−3.51	−3.47

[a] Obtained by laterally constraining the bottommost adsorbate atom.

results, summarized in Fig. S3 of the Supplementary material, show that increasing the Ru–Ru distance by 0.02 Å leads to a slight strengthening of the adsorption binding energy by 0.02 eV in both phases. While this effect is not entirely negligible, it does not explain the difference in top-site binding energies between the two phases.

As for OH adsorption, the most favorable sites are the hcp site on Ru-hcp(001) and the fcc site on Ru-fcc(111), with slightly stronger binding on Ru-hcp(001) (Table 2). A difference in OH binding energy is observed between the two supercell sizes, particularly at hollow sites. As coverage decreases, OH becomes more stable, especially at hollow sites. Further decreasing the coverage has only a negligible effect on the OH adsorption binding energy (Table S4 in the Supplementary material). Similar to H adsorption, the top site is the least favorable for OH, and Ru-hcp(001) binds OH* about 0.1 eV more strongly than Ru-fcc(111). Literature reports on OH adsorption strength are conflicting. Zhao et al. [13] identified the fcc site as the most favorable on both

Ru-hcp(001) and Ru-fcc(111), with slightly stronger binding on Ru-hcp(001). In contrast, Nandi et al. [12] found the hcp site to be most stable, reporting comparable OH binding energies for both surfaces.

From the results presented in Table 2, we conclude that both H and OH preferentially adsorb at hollow sites, exhibiting similar binding energies on Ru-hcp(001) and Ru-fcc(111). The largest difference in adsorption energy between the two surfaces occurs at the top site – approximately 0.1 eV for both species – whereas adsorption at the fcc and bridge sites yields comparable binding strengths for both crystal phases.

3.1.2. Electronic structure analysis of H–Ru bonding

To rationalize the differences in adsorption behavior between Ru-hcp(001) and Ru-fcc(111), we analyzed the PDOS, ILDOS, and COHP for H adsorbed at the top and fcc sites (Fig. 2).

For H adsorption at the fcc site, the H 1s orbital exhibits a sharp, well-defined peak in the energy range from −7 to −6 eV relative to the Fermi energy. The PDOS of the Ru surface atom bonded to H displays a corresponding peak in the same energy range, indicating strong hybridization between the H and Ru electronic states. This is further corroborated by the absence of density of states in this range for the bare Ru surfaces. Visualization of the electronic states associated with this sharp peak via ILDOS (Fig. 2) reveals features resembling tilted d_{z^2}-like orbitals on the Ru atoms, spatially merged with the H 1s orbital; for further details, see the orbital-projected PDOS in Fig. S4 of the Supplementary material. To complement the PDOS and ILDOS interpretation, the COHP analysis shows that the bonding characteristics of H adsorbed at the fcc site are very similar on both surfaces. The COHP curves for Ru-hcp(001) and Ru-fcc(111) exhibit nearly identical features, with only slight differences in the integrated COHP values (−1.27 and −1.30, respectively). Furthermore, Bader charge analysis indicates that the H atom adsorbed at the fcc site on Ru-hcp(001) carries a marginally more negative charge (−0.26) than the corresponding H atom on Ru-fcc(111) (−0.25).

In contrast, at the top site, the sharp peak observed in PDOS of the fcc site is absent. Instead, the Ru–H interaction occurs at higher energies, beginning around −5 eV relative to the Fermi energy. Compared to the bare Ru surface, the Ru atom bonded to H shows an increased PDOS from −6 to −3 eV and a corresponding decrease at higher energies, indicating a downshift of Ru states upon H adsorption. The PDOS projected onto the individual valence orbitals of the Ru atom bonded to H (Fig. S5 in the Supplementary material) reveals that the Ru 5s and $4d_{z^2}$ orbitals are involved in the Ru–H interaction, consistent with the geometry of the top site. While the 5s orbital exhibits a similar PDOS for both surfaces, the $4d_{z^2}$ orbital shows a considerably sharper peak at approximately −4.5 eV for Ru-hcp(001), resulting in stronger H binding at the top site on Ru-hcp(001) compared to Ru-fcc(111). The importance of this Ru–H orbital interaction in determining adsorption strength has previously been reported [41]. Additionally, the calculated COHP curves for H adsorbed at the top site differ between the two surfaces, and the integrated COHP values are slightly lower for Ru-hcp(001) (−2.69) than for Ru-fcc(111) (−2.64), consistent with the stronger adsorption energy. The calculated Bader charges for the H atom adsorbed at the top site are −0.17 on both surfaces.

3.2. Dissociation of adsorbed water

To investigate the mechanism of adsorbed water dissociation, reaction (7), we considered two models: a single adsorbed water molecule and an ice-like water bilayer, using both the $(\sqrt{3}\times\sqrt{3})$R30° and (3×3) supercells.

Table 3
Reaction (ΔE) and activation (E^{act}) energies for the dissociation of a single water molecule on Ru-hcp(001) and Ru-fcc(111), obtained with the $(\sqrt{3}\times\sqrt{3})$R30° and (3×3) supercells for slabs thicker than four layers. N denotes the number of Ru layers in the slab. Energies obtained using implicit-solvent calculations on the vacuum-optimized geometries are shown in parentheses.

supercell	ΔE (eV)		E^{act} (eV)	
N	Ru-hcp(001)	Ru-fcc(111)	Ru-hcp(001)	Ru-fcc(111)
$(\sqrt{3}\times\sqrt{3})$R30°				
5	−0.31 (−0.31)	−0.26 (−0.26)	0.75 (0.79)	0.77 (0.82)
6	−0.22 (−0.21)	−0.28 (−0.28)	0.75 (0.81)	0.76 (0.81)
7	−0.21 (−0.22)	−0.25 (−0.26)	0.75 (0.80)	0.76 (0.81)
(3×3)				
5	−0.50 (−0.42)	−0.42 (−0.35)	0.78 (0.93)	0.79 (0.94)
6	−0.46 (−0.37)	−0.46 (−0.40)	0.80 (0.97)	0.78 (0.93)
7	−0.46 (−0.37)	−0.44 (−0.37)	0.79 (0.95)	0.79 (0.94)

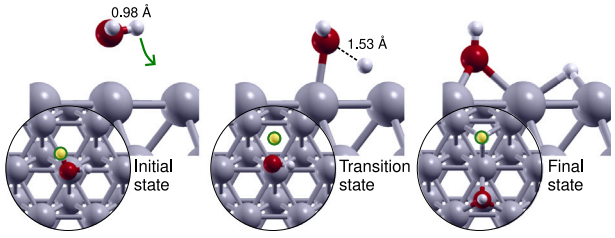

Fig. 3. Top- and side-view snapshots of the IS, TS, and FS structures for H_2O dissociation on Ru-hcp(001)–(3×3). In the side-view IS snapshot, the direction of the dissociating H atom is marked with a green arrow, whereas in the top-view snapshots the H atom is highlighted in green–yellow. (For interpretation of the references to color in this figure legend, the reader is referred to the web version of this article.)

3.2.1. A single water molecule

A single water molecule preferentially adsorbs at the top site, with both O–H bonds lying parallel to the surface. The most stable final state after dissociation has both OH and H fragments adsorbed at fcc sites in the smaller $(\sqrt{3}\times\sqrt{3})$R30° supercell. In contrast, in the larger (3×3) supercell, the configuration with OH at the hcp site and H at the fcc site is more stable (see Fig. S6 in the Supplementary material). The reaction coordinate for water dissociation primarily involves the elongation of an O–H bond from 0.98 Å in the IS to 1.53 Å in the TS, with the O atom shifting slightly off the top site and the H atom positioned above the fcc site. The calculated reaction and activation energies are listed in Table 3, representative IS, TS, and FS structures are shown in Fig. 3, and the reaction paths for all considered systems are presented in Figs. S9–S20 of the Supplementary material.

As shown in the preceding section, 3- and 4-layer slabs are not converged with respect to adsorption binding energies, so only slabs thicker than four layers are considered here. Table 3 further shows that the 5-layer slab likewise does not yield converged reaction energies and is therefore excluded from the following discussion, although its activation energies are nearly identical to those of thicker slabs. For the smaller $(\sqrt{3}\times\sqrt{3})$R30° supercell, reaction energies are moderately more exothermic on Ru-fcc(111), whereas for the larger (3×3) supercell, they are similar on both Ru-hcp(001) and Ru-fcc(111). The latter trend is consistent with the adsorption energies in Table 2, which indicate comparable H and OH binding strengths at hollow sites on both surfaces. Decreasing the OH and H coverages below 1/9 ML does not affect the reaction and activation energies (see Table S4); therefore, the results from the (3×3) supercell can be regarded as representative of the low-coverage limit.

Despite the differences in reaction energies between Ru-hcp(001) and Ru-fcc(111), the calculated activation energies are very similar for the two surfaces and show little sensitivity to slab thickness, with values

of about 0.75 eV for the smaller and 0.80 eV for the larger supercell. In detail, for the smaller $(\sqrt{3}\times\sqrt{3})$R30° supercell, the activation energy is 0.01 eV lower on Ru-hcp(001), whereas, for the larger (3×3) supercell, both surfaces yield the value of 0.79 eV. This similarity in activation energies is consistent with the fact that the transition-state structures are alike for all systems considered, as shown in Figs. S9–S20 in the Supplementary material.

In addition to the *in-vacuo* calculations, we also performed calculations with an implicit aqueous solvent on the geometries optimized in vacuum. The corresponding reaction and activation energies for the dissociation of a single water molecule on Ru-hcp(001) and Ru-fcc(111) are shown in parentheses in Table 3. For the smaller $(\sqrt{3}\times\sqrt{3})$R30° supercell, the reaction energies are similar to those in vacuum, whereas the activation energies are 0.05 ± 0.01 eV higher. In contrast, for the (3×3) supercell, the changes are more pronounced. In particular, the reaction energies obtained with the implicit solvent are 0.08 ± 0.01 eV less exothermic, while the activation energies are 0.16 ± 0.01 eV higher. This indicates that, within the implicit solvent model, the initial state is more strongly stabilized than the transition and final states. It is noteworthy that despite these solvent-induced changes, the trends between the Ru-hcp(001) and Ru-fcc(111) surfaces remain unchanged. However, the implicit solvent model does not include directional hydrogen bonding between water molecules. Therefore, we also modeled water explicitly using a simple ice-like bilayer, which incorporates surrounding water molecules and places water molecules within a hydrogen-bonded network.

3.2.2. Ice-like water bilayer

A widely used model of interfacial water at solid/water interfaces is the ice-like water bilayer, in which water molecules are connected via hydrogen bonds. The smaller $(\sqrt{3}\times\sqrt{3})$R30° supercell contains two water molecules, resulting in a highly symmetric and constrained bilayer. In contrast, the larger (3×3) supercell contains six water molecules, allowing a more flexible arrangement.

We tested different trajectories for the dissociating H atom during O–H bond cleavage, as illustrated in Fig. 4a. In the $(\sqrt{3}\times\sqrt{3})$R30° supercell, the dissociating H atom can proceed along three distinct directions, denoted as −60°, 60°, and 180°, where the angles are defined relative to the xy projection of the non-dissociating O–H bond (marked with a black dotted line in Fig. 4a). The −60° and 60° reaction paths are very similar,[2] and yield nearly identical activation energies, differing by less than 0.01 eV. Consequently, the −60° path is omitted from further consideration. In the (3×3) supercell, the resulting H* is more stable at a bridge-like adsorption site. Two geometrically favorable dissociation directions were identified, denoted as 90° and 150°, corresponding to the 60° and 180° directions in the smaller supercell, respectively. For the 90° pathway, in addition to O–H bond cleavage, a proton is transferred from a neighboring water molecule to the dissociating one, as indicated by the smaller arrow in Fig. 4a.

For both supercells, dissociation of a water molecule results in OH at a top site for all tested pathways. In contrast, the H adsorption site depends on the supercell size: in the smaller cell it binds to a nearby top site, while in the larger cell it occupies a bridge-like site as the surrounding water network can reorganize (Fig. 5). A detailed visualization of the H-atom trajectories during water dissociation on Ru-hcp(001) for the considered pathways is shown in Fig. 4b. The corresponding trajectories on Ru-fcc(111) are similar (not shown). In all cases, the H atom passes through a bridge-like site in the transition state. Representative IS, TS, and FS structures are shown in Fig. 5, and the corresponding reaction profiles, together with these structures for all considered systems, are presented in Figs. S21–S52 in the Supplementary material.

[2] The difference between the −60° and 60° pathways is that the dissociating H atom, while moving to the adjacent top site, passes by the hcp and fcc sites, respectively.

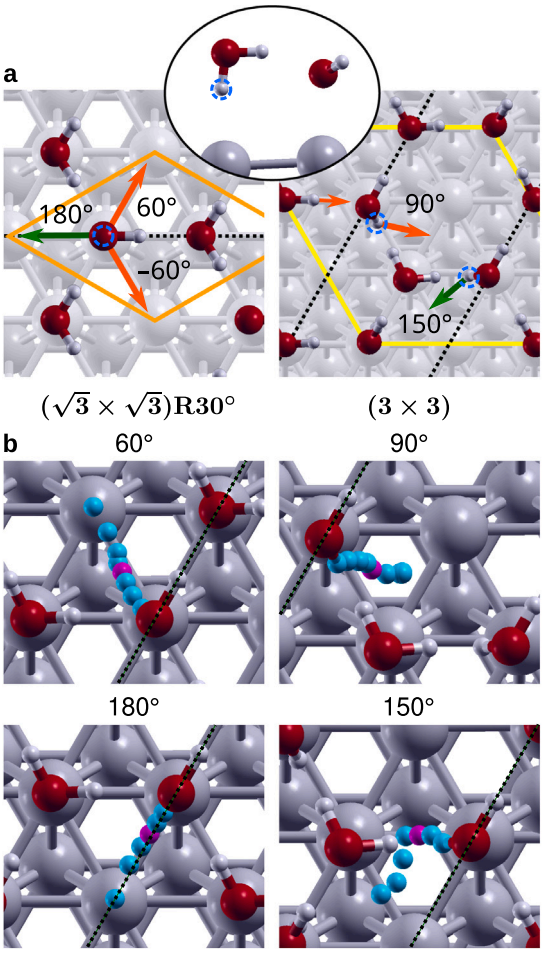

Fig. 4. Dissociation pathways of a water molecule within a water bilayer on a Ru surface for the $(\sqrt{3}\times\sqrt{3})$R30° and (3×3) supercells. (a) Schematic illustration of the direction of the dissociating H atom (marked by arrows); the angle is measured relative to the non-dissociating O–H bond (black dotted lines). For the 90° trajectory in the (3×3) supercell, a proton transfer from a neighboring water molecule occurs during dissociation (indicated by a smaller orange arrow). (b) Trajectories of the dissociating H atom shown as blue balls, with its transition-state position highlighted in purple. (For interpretation of the references to color in this figure legend, the reader is referred to the web version of this article.)

Calculated reaction and activation energies for the $(\sqrt{3}\times\sqrt{3})$R30° supercell are presented in Table 4, and the corresponding reaction pathways are shown in Figs. S21–S40 in the Supplementary material. For both investigated trajectories, the initial and final states are identical, resulting in the same reaction energies. The results for Ru-hcp(001) are largely insensitive to slab thickness, whereas those for Ru-fcc(111) converge more slowly and require slabs at least five layers thick. This trend agrees with the convergence behavior observed for the adsorption energies in Table 1. For this reason, thin-slab results are discarded in the below discussion.

Ru-hcp(001) exhibits reaction energies about 0.2–0.3 eV more exothermic than Ru-fcc(111). Since the two surfaces differ only in their stacking sequence, this difference appears large but can largely be attributed to adsorption energy differences. Namely, in the smaller cell, both H and OH are adsorbed at top sites, which bind more strongly on Ru-hcp(001).

Despite this substantial difference in reaction energies, the activation energies are quite similar for the two surfaces, with the 60° trajectory showing about 0.1 eV lower values. For this preferred trajectory,

Table 4
The ($\sqrt{3}\times\sqrt{3}$)R30° reaction and activation energies for the H_2O dissociation reaction on Ru-hcp(001) and Ru-fcc(111) calculated with the water bilayer model along the 60° and 180° reaction paths. Values in parentheses correspond to calculations where only the topmost three layers were relaxed; all other values correspond to calculations in which only the bottommost Ru layer was fixed. Note that the ΔE values for the 60° and 180° trajectories are identical, as both have equivalent initial and final states.

	ΔE (eV)		60° trajectory E^{act} (eV)		180° trajectory E^{act} (eV)	
N	Ru-hcp(001)	Ru-fcc(111)	Ru-hcp(001)	Ru-fcc(111)	Ru-hcp(001)	Ru-fcc(111)
3	−0.60	−0.13	0.43	0.51	0.58	0.63
4	−0.61	−0.48	0.40	0.43	0.54	0.57
5	−0.60 (−0.58)	−0.31 (−0.31)	0.44	0.49	0.57	0.61
6	−0.59 (−0.58)	−0.35 (−0.35)	0.46	0.47	0.59	0.58
7	−0.59 (−0.58)	−0.36 (−0.35)	0.43	0.47	0.56	0.58

Table 5
The (3 × 3) reaction and activation energies for the H_2O dissociation reaction on Ru-hcp(001) and Ru-fcc(111) calculated with the water bilayer model along the 90° and 150° reaction paths.

	90° trajectory ΔE (eV)		E^{act} (eV)		150° trajectory ΔE (eV)		E^{act} (eV)	
N	Ru-hcp(001)	Ru-fcc(111)	Ru-hcp(001)	Ru-fcc(111)	Ru-hcp(001)	Ru-fcc(111)	Ru-hcp(001)	Ru-fcc(111)
5	−0.73	−0.55	0.53	0.57	−0.36	−0.23	0.52	0.60
6	−0.70	−0.60	0.52	0.54	−0.33	−0.25	0.55	0.57
7	−0.73	−0.59	0.51	0.55	−0.35	−0.25	0.52	0.57

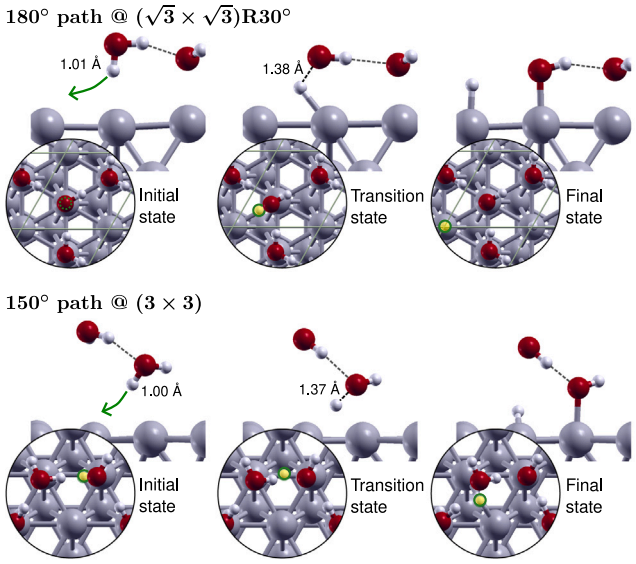

Fig. 5. Top- and side-view snapshots of the IS, TS, and FS structures for H_2O dissociation within a water bilayer on Ru-hcp(001), shown for the 180° path in the ($\sqrt{3}\times\sqrt{3}$)R30° supercell (top) and for the 150° path in the (3 × 3) supercell (bottom). In the side-view IS, the direction of the dissociating H atom is marked with a green arrow, whereas in the top-view snapshots the H atom is highlighted in green–yellow. (For interpretation of the references to color in this figure legend, the reader is referred to the web version of this article.)

Ru-hcp(001) has a slightly lower activation energy than Ru-fcc(111), by an average of 0.03 eV for slabs at least five layers thick.

For the (3 × 3) supercell, the results are shown in Table 5, and the corresponding reaction paths are given in Figs. S41–S52. The initial states are identical for both considered paths, but the final states differ, leading to significant variation in the calculated reaction energies. The 90° path is considerably more exothermic than the 150° path on both Ru surfaces. In the 90° case, an H atom is transferred from a neighboring water molecule to the dissociating one (Figs. S47–S52), meaning that the original water molecule remains intact, whereas the neighboring molecule converts into OH*. This H-atom transfer increases the separation between the resulting OH* and H* species and thereby stabilizes the final state. An annotated snapshot of this concomitant water dissociation and proton-hopping process is shown in Fig. S7 in the Supplementary material together with the associated Bader charge analysis, which reveals that the hopping H atom is proton-like, whereas the dissociating H atom transforms from a proton-like to a hydride-like state.

For both reaction paths in the (3×3) supercell, Ru-hcp(001) exhibits reaction energies about 0.1 eV more exothermic than Ru-fcc(111). This difference is smaller than in the smaller supercell and can be attributed to the final-state structure: only OH is adsorbed at the top site, where adsorption energy differs significantly between the two surfaces, while H occupies a bridge-like site with similar adsorption energy on both surfaces.

In contrast to the reaction energies, no large differences are observed between the activation energies on Ru-hcp(001) and Ru-fcc(111) for the (3 × 3) supercell. The two reaction paths also yield similar activation energies, with the 90° path displaying marginally smaller values. For this slightly preferred path, Ru-hcp(001) has a slightly lower activation energy than Ru-fcc(111), by an average of 0.02 eV for slabs at least five layers thick.

The activation energy results for thicker slabs, presented in Tables 4 and 5, therefore indicate that Ru-hcp(001) exhibits slightly lower activation barriers for both supercells. Furthermore, the water molecule prefers to dissociate along a more *angular* trajectory—corresponding to the 60° path for the smaller ($\sqrt{3}\times\sqrt{3}$)R30° supercell and the 90° path for the larger (3 × 3) supercell. This preference was also reported by Zheng et al. [14], although in that work the more *angular* path was rejected due to the absence of an imaginary frequency in the NEB-identified transition state. In contrast, our vibrational analysis reveals one imaginary frequency for the transition state of each path, confirming them as viable options.

3.3. Activation and reaction Gibbs energies

The results and analysis presented above are based on activation and reaction energies calculated at 0 K without ZPE. However, for evaluating reaction kinetics and thermodynamics, the relevant quantities are the activation and reaction Gibbs energies calculated under experimental conditions. We therefore now turn to these, using the thermodynamic framework described in Technical Section 2.1.

Because vibrational calculations are computationally demanding, they were performed only for the ice-like water bilayer models. For the

Table 6
Reaction (ΔG) and activation (G^{act}) Gibbs energies calculated at 25 °C for the $(\sqrt{3}\times\sqrt{3})$R30° supercell with the ice-like water bilayer model. The G^{act} values are reported for the 60° and 180° paths, while the ΔG values are identical for both paths. The G_{corr} corrections of Eq. (6), labeled as ΔG_{corr} and G^{act}_{corr}, which transform 0 K energies into Gibbs energies, are also reported. N denotes the number of Ru layers in the slab.

	ΔG (eV)		ΔG_{corr} (eV)		60° trajectory G^{act} (eV)		G^{act}_{corr} (eV)		180° trajectory G^{act} (eV)		G^{act}_{corr} (eV)	
N	hcp(001)	fcc(111)	hcp(001)	fcc(111)	hcp(001)	fcc(111)	hcp(001)	fcc(111)	hcp(001)	fcc(111)	hcp(001)	fcc(111)
3	−0.59	−0.17	0.004	−0.040	0.32	0.40	−0.112	−0.116	0.44	0.50	−0.135	−0.131
4	−0.59	−0.47	0.017	+0.007	0.30	0.32	−0.100	−0.109	0.42	0.44	−0.119	−0.125
5	−0.58	−0.32	0.025	−0.017	0.33	0.37	−0.106	−0.112	0.44	0.49	−0.123	−0.122
6[a]	−0.56	−0.36	/	/	0.35	0.36	/	/	0.46	0.46	/	/
7[a]	−0.56	−0.38	/	/	0.32	0.35	/	/	0.44	0.46	/	/

[a] The ΔG and G^{act} values were obtained by combining the ΔE and E^{act} values with the corresponding G_{corr} corrections from the five-layer slab.

Table 7
Reaction (ΔG) and activation (G^{act}) Gibbs energies of the 90° path calculated at 25 °C for the (3×3) supercell with the ice-like water bilayer model. The ΔG_{corr} and G^{act}_{corr} corrections were approximated by calculating and diagonalizing only the water-bilayer part of the interatomic force-constants matrix.

	ΔG (eV)		ΔG_{corr} (eV)		G^{act} (eV)		G^{act}_{corr} (eV)	
N	hcp(001)	fcc(111)	hcp(001)	fcc(111)	hcp(001)	fcc(111)	hcp(001)	fcc(111)
5	−0.83	−0.65	−0.096	−0.099	0.35	0.39	−0.181	−0.185
6[a]	−0.80	−0.70	/	/	0.34	0.35	/	/
7[a]	−0.83	−0.69	/	/	0.33	0.36	/	/

[a] The ΔG and G^{act} values were obtained by combining the ΔE and E^{act} values with the corresponding G_{corr} corrections from the five-layer slab.

smaller $(\sqrt{3}\times\sqrt{3})$R30° supercell, both considered paths were analyzed on slabs three to five layers thick by calculating and diagonalizing the full interatomic force-constants matrix. For thicker slabs, we used the vibrational contributions to the Gibbs energy derived from the five-layer slab. In contrast, for the larger (3×3) supercell, only the five-layer slabs for the 90° trajectory were analyzed by calculating and diagonalizing only the water-bilayer part of the interatomic force-constants matrix.

All considered transition states exhibit a single imaginary frequency of approximately 1000 i cm^{-1}, corresponding to the reaction coordinate. This mode was excluded from the vibrational contribution, as prescribed by transition-state theory. The resulting activation (G^{act}) and reaction Gibbs energies (ΔG) calculated at 25 °C, along with the vibrational corrections of Eq. (6) that transform 0 K energies into Gibbs energies, labeled as ΔG_{corr} and G^{act}_{corr}, respectively, are tabulated in Table 6 for the $(\sqrt{3}\times\sqrt{3})$R30° supercell and in Table 7 for the (3×3) supercell. Furthermore, the G^{act} and ΔG values are illustrated in Fig. 6, which compares them with the corresponding activation and reaction energies at 0 K. Note that for $(\sqrt{3}\times\sqrt{3})$R30° both the 60° and 180° reaction paths start from the same initial state and end in the same final state, differing only in the H trajectory during the O–H bond cleavage. Consequently, the two trajectories have identical reaction Gibbs energies but different activation Gibbs energies.

For the $(\sqrt{3}\times\sqrt{3})$R30° supercell, the vibrational contributions (ΔG_{corr}) to the reaction Gibbs energies are small in magnitude, ranging from −0.04 to +0.03 eV, which indicates that they largely cancel between the final and initial states. In contrast, for the (3×3) supercell, the ΔG_{corr} values are about −0.1 eV for both Ru-fcc(111) and Ru-hcp(001). Comparing these corrections between Ru-fcc(111) and Ru-hcp(001), we realize that their differences are small compared with the reaction energy differences. Thus, the reaction Gibbs energies follow the same trend as the reaction energies. These ΔG values correspond to the dissociation of an adsorbed water molecule, reaction (7). At the RHE potential, they can be mapped onto the Gibbs energies of the Volmer reaction (1), ΔG_{Volmer}, using Eq. (S6), which is based on the thermodynamic cycle in Scheme S1. Our calculations show that $\Delta G_{Volmer} = \Delta G - 0.07$ eV for Ru-hcp(001) and $\Delta G_{Volmer} = \Delta G - 0.13$ eV for Ru-fcc(001). The corresponding ΔG_{Volmer} values are given in Table S5 of the Supplementary material.

In contrast to the reaction Gibbs energies, all vibrational contributions (G^{act}_{corr}) to the activation Gibbs energies are negative: about −0.1 eV for $(\sqrt{3}\times\sqrt{3})$R30° on both surfaces and about −0.2 eV for (3×3) on both surfaces. Because the G^{act}_{corr} values are similar for Ru-fcc(111) and Ru-hcp(001), these contributions do not change the activation energy trend established in the preceding section. Consequently, Ru-hcp(001) exhibits slightly lower activation Gibbs energies than Ru-fcc(111). This trend is not affected by slab thickness, as all thicknesses consistently reveal it. More specifically, for the $(\sqrt{3}\times\sqrt{3})$R30° supercell, the activation Gibbs energies for the preferred 60° path are 0.33 and 0.36 eV for Ru-hcp(001) and Ru-fcc(111), respectively, calculated as the average over the five- to seven-layer slabs. The corresponding values for the 180° path are 0.44 and 0.47 eV. For the (3×3) supercell, the values for the 90° path are 0.34 and 0.37 eV for Ru-hcp(001) and Ru-fcc(111).

The presented results contrast with the high-impact study of Zheng et al. [14], who attributed the experimentally observed higher activity of the Ru-fcc phase to a DFT-calculated higher intrinsic activity of Ru-fcc(111) compared with Ru-hcp(001). They used three-layer Ru slabs along with the bilayer model of water and the $(\sqrt{3}\times\sqrt{3})$R30° supercell. While their reaction Gibbs energies of −0.59 and −0.24 eV for Ru-hcp(001) and Ru-fcc(111), respectively,[3] follow a similar trend to ours (cf. Table 6 and Fig. 6) – namely, that the water dissociation reaction is significantly more exergonic on Ru-hcp(001) – their reported activation Gibbs energies of 0.51 and 0.41 eV for the 180° path on Ru-hcp(001) and Ru-fcc(111), respectively, are in stark contrast to our results. While their calculations suggest that Ru-fcc(111) is considerably more active than Ru-hcp(001), our results indicate that Ru-hcp(001) is in fact more active.

Zheng et al. [14] reported vibrational contributions to the activation Gibbs energy of +0.03 eV for Ru-hcp(001) and −0.10 eV for Ru-fcc(111), whereas our $(\sqrt{3}\times\sqrt{3})$R30° value is approximately −0.10 eV for both surfaces. This discrepancy arises from two sources: (a) the incomplete treatment of vibrational contributions in their work, and (b) their use of too-thin slabs, which lead to unconverged results as demonstrated above. Specifically, their incomplete treatment of vibrational contributions has three shortcomings:

(i) Only the zero-point energy (ZPE) was considered, while thermal contributions to the vibrational Gibbs energy were neglected. In

[3] Zheng et al. [14] reported only the Volmer-step Gibbs energies, ΔG_{Volmer} = −0.84 and −0.48 eV, which were derived from the ΔG energies of reaction (7) using $\Delta G_{Volmer} = \Delta G - 0.24$ eV for both Ru-hcp(001) and Ru-fcc(111).

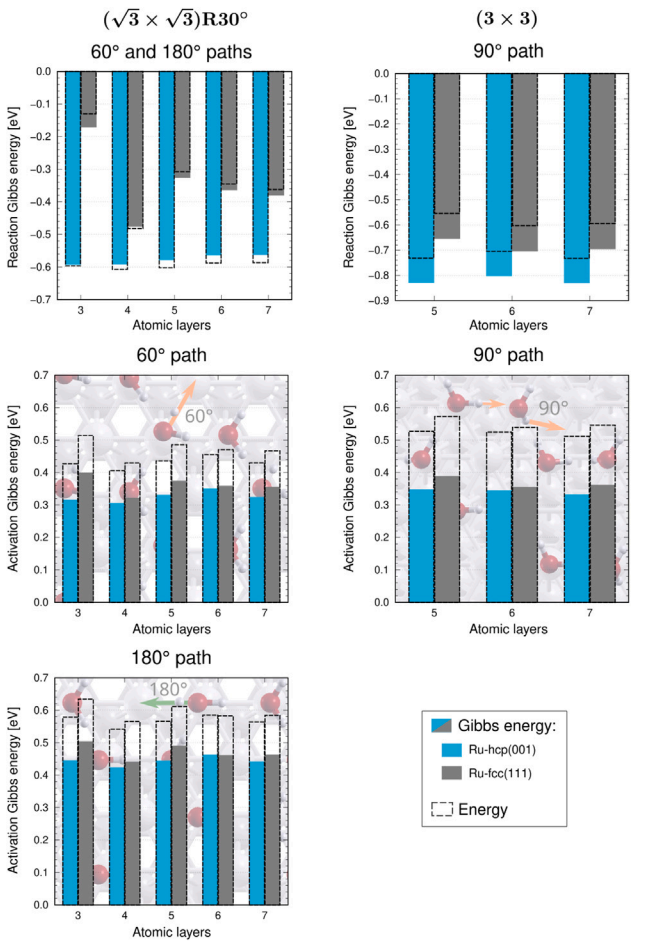

Fig. 6. The $(\sqrt{3}\times\sqrt{3})$R30° (left) and (3×3) (right) reaction and activation Gibbs energies for H_2O dissociation, calculated at 25 °C using the water bilayer model. Results for Ru-hcp(001) are shown in blue and for Ru-fcc(111) in grey. Gibbs energies are represented by solid colored bars, while the corresponding energies are indicated by black dashed bars. Note that for the $(\sqrt{3}\times\sqrt{3})$R30° supercell, the reaction Gibbs energies are identical for the 60° and 180° paths (top left). (For interpretation of the references to color in this figure legend, the reader is referred to the web version of this article.)

particular, Zheng et al. used $E_{\mathrm{vib}}(T) = \frac{1}{2}\sum_i h\nu_i \equiv \mathrm{ZPE}$, whereas the correct harmonic-oscillator expression is:

$$E_{\mathrm{vib}}(T) = \sum_i h\nu_i \left(\frac{1}{2} + \frac{1}{\exp(\frac{h\nu_i}{k_B T}) - 1} \right). \tag{8}$$

It is worth emphasizing that for low-frequency modes the thermal term becomes larger than the ZPE term (for example, for $h\nu = k_B T/2$, the second term is about 1.5, i.e., three times larger than the first term).

(ii) In the harmonic-oscillator model, vibrational entropy diverges as the frequency approaches zero. Without correcting for this effect, low-frequency modes contribute excessively to the vibrational Gibbs energy, potentially leading to nonphysical results. Zheng et al. applied no correction for the low-frequency modes, whereas we used the Cramer–Truhlar correction [35]. An analysis of how the Cramer–Truhlar correction affects the activation and reaction Gibbs energies is presented in Fig. S8 in the Supplementary material. This analysis shows that the apparent preference for Ru-fcc(111) over Ru-hcp(001) in the work of Zheng et al. arises primarily from a super-soft vibrational mode of 4 cm^{-1} in the initial state on Ru-hcp(001), whereas the corresponding mode on Ru-fcc(111) is 42 cm^{-1}. Because vibrational entropy diverges for very low frequencies, the 4 cm^{-1} mode contributes excessively to the entropic term on Ru-hcp(001), artificially stabilizing the initial state and thereby increasing both the activation and reaction Gibbs energies on Ru-hcp(001) relative to Ru-fcc(111).

(iii) Zheng et al. [14] diagonalized only the adsorbate part of the interatomic force-constants matrix, whereas we calculated and diagonalized the full matrix. According to our calculations, this approximation introduces errors of about 0.02 eV for the activation Gibbs energy and 0.05 eV for the reaction Gibbs energy in the present case (see Table S6).

For the results reported by Zhang et al. using the full vibrational thermal energy from Eq. (8) instead of only the ZPE yields vibrational contributions to the activation Gibbs energy of −0.01 eV for Ru-hcp(001) and −0.12 eV for Ru-fcc(111). Including the Cramer–Truhlar correction for the low-frequency modes gives the corresponding values of −0.09 and −0.14 eV. Thus, a more comprehensive treatment reduces the difference in vibrational contributions between Ru-hcp(001) and Ru-fcc(111) from 0.13 eV to 0.05 eV, and consequently reduces the fcc vs. hcp preference from 0.10 eV to only 0.02 eV. In other words, their original activation Gibbs energies of 0.51 and 0.41 eV for Ru-hcp(001) and Ru-fcc(111), respectively, are corrected to 0.39 and 0.37 eV.

Further improvement of these values is achieved by using the full interatomic force-constants matrix instead of only the adsorbate part, and by employing thicker slab models. Addressing all these issues results in similar vibrational contributions of about −0.1 eV to the activation Gibbs energy for Ru-hcp(001) and Ru-fcc(111), as obtained with the $(\sqrt{3}\times\sqrt{3})$R30° supercell. Vibrational contributions to the activation Gibbs energies remain similar between the two surfaces when calculated with the larger (3×3) supercell, which is more realistic because dissociation of water molecules occurs individually at specific sites and times. For these four reasons, we place greater confidence in our results than in those of Zheng et al. [14].

3.4. Activity of Ru-hcp(001) and Ru-fcc(111) and implications for supported nanoparticle catalysts

Based on our results and the identified shortcomings in the DFT study by Zheng et al. [14], we argue that the ideal Ru-fcc(111) surface is not intrinsically more active than Ru-hcp(001). On the contrary, our findings suggest that Ru-hcp(001) should be more active toward the water dissociation reaction. At room temperature, a difference of 0.03 eV in the activation Gibbs energy corresponds to a change in the reaction rate by approximately a factor of three, illustrating that even small variations in activation energies substantially influence reaction kinetics. However, a difference of 0.03 eV is itself small within the accuracy of typical DFT calculations. Hence, conclusions drawn from it should be considered with due caution.

Our results are based on approximating the Volmer reaction step by a nonelectrochemical dissociation of an adsorbed water molecule and on the use of oversimplified water models. Further computational investigation of the experimentally observed higher HER activity of Ru-fcc nanoparticles compared to Ru-hcp ones, using more realistic electrochemical models, is therefore needed to obtain a more reliable assessment of their relative activities under experimental conditions.

Based on the presented results, we question the previously proposed explanation [14] that the experimentally observed higher HER activity of Ru-fcc nanoparticles relative to Ru-hcp ones arises from differences in the intrinsic activity of the close-packed Ru-hcp(001) and Ru-fcc(111) surfaces. When moving from ideal surfaces to real catalysts, factors such as nanoparticle shape, the reactivity of less stable facets, and the fraction of exposed facets may also play decisive roles, as demonstrated for CO dissociation on Ru [9,10]. The stability of different facets – and thus the distribution of exposed facets – also depends

on reaction conditions, since changes in adsorbate coverage can modify facet populations and affect overall nanoparticle activity [10]. Another important factor could be the influence of the support, particularly when the fcc phase is grown on a support different from that of the reference hcp system, as this may alter nanoparticle–support interactions and thereby affect reactivity toward key intermediates [42].

This work therefore provides an initial step toward understanding the different activities of supported Ru-hcp and Ru-fcc nanoparticles and shows that the previously proposed explanation [14] is unlikely. Further studies focusing on facet-specific activity and support effects will be essential for definitively clarifying the origins of the experimentally observed enhanced HER activity of supported Ru-fcc nanoparticles and for guiding the design of more efficient catalyst systems.

4. Conclusion

This work provides a comparative DFT perspective on the activity of Ru-hcp(001) and Ru-fcc(111) surfaces toward water dissociation, a key step in the hydrogen evolution reaction in alkaline media. By analyzing both single-molecule and bilayer water models, we showed that reaction energies depend strongly on slab thickness, supercell size, and the water model, whereas the activation barriers are less sensitive to these details. These findings underscore the importance of employing sufficiently converged computational models in order to obtain reliable and meaningful results.

Despite these sensitivities, the overall picture is robust: water dissociation is predicted to be more exergonic and to have slightly lower activation Gibbs energies on Ru-hcp(001), suggesting it should be somewhat more active than Ru-fcc(111). Importantly, vibrational contributions do not alter the relative energy trends, in contrast to earlier work, whose reported data show favorable vibrational contributions of Ru-fcc(111), thereby suggesting its superiority. This difference in vibrational results stems from how vibrational effects were treated, with the earlier study using a less complete approach.

Taken together, our results indicate that the experimentally observed higher activity of fcc-structured Ru nanoparticles in alkaline HER cannot be explained by the intrinsic properties of the Ru-fcc(111) and Ru-hcp(001) facets. Instead, it is likely driven by other factors, such as support effects, facet-specific activity, and facet distribution (i.e., nanoparticle shape). Future studies should therefore place greater emphasis on realistic nanoparticle models and on the role of the support in shaping catalytic performance.

CRediT authorship contribution statement

Lea Gašparič: Writing – review & editing, Writing – original draft, Visualization, Methodology, Investigation, Formal analysis, Conceptualization. **Anton Kokalj:** Writing – review & editing, Supervision, Project administration, Formal analysis, Conceptualization.

AI use statement

The authors used ChatGPT (developed by OpenAI) to assist with language editing. All content was created and reviewed by the authors, who takes full responsibility for the integrity and accuracy of the manuscript.

Declaration of competing interest

The authors declare that they have no known competing financial interests or personal relationships that could have appeared to influence the work reported in this paper.

Acknowledgments

The authors thank the eletrocatalysis group at the National Institute of Chemistry, especially M. Smiljanić for his collaboration and for introducing the topic of the catalytic activity of fcc Ru. This work was financially supported by the Slovenian Research and Innovation Agency (Grant Nos. P2-0393 and J7-4637).

Appendix A. Supplementary data

Supplementary material related to this article can be found online at https://doi.org/10.1016/j.jcat.2025.116641.

Data availability

Data will be made available on request.

References

[1] L. Li, F. Tian, L. Qiu, F. Wu, W. Yang, Y. Yu, Recent progress on ruthenium-based electrocatalysts towards the hydrogen evolution reaction, Catalysts 13 (12) (2023) 1497, http://dx.doi.org/10.3390/catal13121497.
[2] L. Hou, H. Jang, X. Gu, X. Cui, J. Tang, J. Cho, X. Liu, Design strategies of ruthenium-based materials toward alkaline hydrogen evolution reaction, EcoEnergy 1 (1) (2023) 16–44, http://dx.doi.org/10.1002/ece2.4.
[3] S.-Y. Bae, J. Mahmood, I.-Y. Jeon, J.-B. Baek, Recent advances in ruthenium-based electrocatalysts for the hydrogen evolution reaction, Nanoscale Horiz. 5 (1) (2020) 43–56, http://dx.doi.org/10.1039/C9NH00485H.
[4] W. Luo, Y. Wang, C. Cheng, Ru-based electrocatalysts for hydrogen evolution reaction : Recent research advances and perspectives, Mater. Today Phys. 15 (2020) 100274, http://dx.doi.org/10.1016/j.mtphys.2020.100274.
[5] W.-G. Cui, F. Gao, G. Na, X. Wang, Z. Li, Y. Yang, Z. Niu, Y. Qu, D. Wang, H. Pan, Insights into the pH effect on hydrogen electrocatalysis, Chem. Soc. Rev. 53 (20) (2024) 10253–10311, http://dx.doi.org/10.1039/D4CS00370E.
[6] L. Rebollar, S. Intikhab, N.J. Oliveira, Y. Yan, B. Xu, I.T. McCrum, J.D. Snyder, M.H. Tang, "Beyond adsorption" descriptors in hydrogen electrocatalysis, ACS Catal. 10 (24) (2020) 14747–14762, http://dx.doi.org/10.1021/acscatal.0c03801.
[7] N. Govindarajan, A. Xu, K. Chan, How pH affects electrochemical processes, Science 375 (6579) (2022) 379–380, http://dx.doi.org/10.1126/science.abj2421.
[8] K. Kusada, H. Kobayashi, T. Yamamoto, S. Matsumura, N. Sumi, K. Sato, K. Nagaoka, Y. Kubota, H. Kitagawa, Discovery of face-centered-cubic ruthenium nanoparticles: Facile size-controlled synthesis using the chemical reduction method, J. Am. Chem. Soc. 135 (15) (2013) 5493–5496, http://dx.doi.org/10.1021/ja311261s.
[9] W.-Z. Li, J.-X. Liu, J. Gu, W. Zhou, S.-Y. Yao, R. Si, Y. Guo, H.-Y. Su, C.-H. Yan, W.-X. Li, Y.-W. Zhang, D. Ma, Chemical insights into the design and development of face-centered cubic ruthenium catalysts for Fischer–Tropsch synthesis, J. Am. Chem. Soc. 139 (6) (2017) 2267–2276, http://dx.doi.org/10.1021/jacs.6b10375.
[10] P. Zhao, Z. Cao, X. Liu, P. Ren, D.-B. Cao, H. Xiang, H. Jiao, Y. Yang, Y.-W. Li, X.-D. Wen, Morphology and reactivity evolution of HCP and FCC Ru nanoparticles under CO atmosphere, ACS Catal. 9 (4) (2019) 2768–2776, http://dx.doi.org/10.1021/acscatal.8b05074.
[11] Y. Nanba, T. Ishimoto, M. Koyama, Structural stability of ruthenium nanoparticles: A density functional theory study, J. Phys. Chem. C 121 (49) (2017) 27445–27452, http://dx.doi.org/10.1021/acs.jpcc.7b08672.
[12] S. Nandi, A.S. Nair, B. Pathak, First principles investigation on the applicability of ruthenium as a potential ORR catalyst, J. Chem. Sci 132 (1) (2019) 2–9, http://dx.doi.org/10.1007/s12039-019-1691-9.
[13] T. Zhao, D. Xiao, Y. Chen, X. Tang, M. Gong, S. Deng, X. Liu, J. Ma, X. Zhao, D. Wang, Boosting alkaline hydrogen electrooxidation on an unconventional fcc-Ru polycrystal, J. Energy Chem. 61 (2021) 15–22, http://dx.doi.org/10.1016/j.jechem.2020.12.008.
[14] Y. Zheng, Y. Jiao, Y. Zhu, L.H. Li, Y. Han, Y. Chen, M. Jaroniec, S.-Z. Qiao, High electrocatalytic hydrogen evolution activity of an anomalous ruthenium catalyst, J. Am. Chem. Soc. 138 (49) (2016) 16174–16181, http://dx.doi.org/10.1021/jacs.6b11291.
[15] K. Chen, Z. Liu, S. Zhu, Y. Liu, Y. Liu, L. Wang, T. Xia, Z. Zhao, H. Gao, S. Cheng, H. Guo, Ruthenium–nickel nanoparticles with unconventional face-centered cubic crystal phase for highly active electrocatalytic hydrogen evolution, Adv. Funct. Mater. 34 (44) (2024) 2406259, http://dx.doi.org/10.1002/adfm.202406259.
[16] L. Li, C. Liu, S. Liu, J. Wang, J. Han, T.-S. Chan, Y. Li, Z. Hu, Q. Shao, Q. Zhang, X. Huang, Phase engineering of a ruthenium nanostructure toward high-performance bifunctional hydrogen catalysis, ACS Nano 16 (9) (2022) 14885–14894, http://dx.doi.org/10.1021/acsnano.2c05776.

[17] K. Gao, Y. Wang, Z. Wang, Z. Zhu, J. Wang, Z. Luo, C. Zhang, X. Huang, H. Zhang, W. Huang, Ru nanodendrites composed of ultrathin fcc/hcp nanoblades for the hydrogen evolution reaction in alkaline solutions, Chem. Commun. 54 (36) (2018) 4613–4616, http://dx.doi.org/10.1039/C8CC01343H.

[18] Y. Li, L.A. Zhang, Y. Qin, F. Chu, Y. Kong, Y. Tao, Y. Li, Y. Bu, D. Ding, M. Liu, Crystallinity dependence of ruthenium nanocatalyst toward hydrogen evolution reaction, ACS Catal. 8 (7) (2018) 5714–5720, http://dx.doi.org/10.1021/acscatal.8b01609.

[19] P. Giannozzi, S. Baroni, N. Bonini, M. Calandra, R. Car, C. Cavazzoni, D. Ceresoli, G.L. Chiarotti, M. Cococcioni, I. Dabo, A. Dal Corso, S. de Gironcoli, S. Fabris, G. Fratesi, R. Gebauer, U. Gerstmann, C. Gougoussis, A. Kokalj, M. Lazzeri, L. Martin-Samos, N. Marzari, F. Mauri, R. Mazzarello, S. Paolini, A. Pasquarello, L. Paulatto, C. Sbraccia, S. Scandolo, G. Sclauzero, A.P. Seitsonen, A. Smogunov, P. Umari, R.M. Wentzcovitch, QUANTUM ESPRESSO: a modular and open-source software project for quantum simulations of materials, J. Phys.: Condens. Matter. 21 (39) (2009) 395502, http://dx.doi.org/10.1088/0953-8984/21/39/395502, code available from http://www.quantum-espresso.org/.

[20] P. Giannozzi, O. Andreussi, T. Brumme, O. Bunau, M.B. Nardelli, M. Calandra, R. Car, C. Cavazzoni, D. Ceresoli, M. Cococcioni, N. Colonna, I. Carnimeo, A.D. Corso, S. de Gironcoli, P. Delugas, R. DiStasio, A. Ferretti, A. Floris, G. Fratesi, G. Fugallo, R. Gebauer, U. Gerstmann, F. Giustino, T. Gorni, J. Jia, M. Kawamura, H.-Y. Ko, A. Kokalj, E. Küçükbenli, M. Lazzeri, M. Marsili, N. Marzari, F. Mauri, N.L. Nguyen, H.-V. Nguyen, A.O. de-la Roza, L. Paulatto, S. Poncé, D. Rocca, R. Sabatini, B. Santra, M. Schlipf, A.P. Seitsonen, A. Smogunov, I. Timrov, T. Thonhauser, P. Umari, N. Vast, X. Wu, S. Baroni, Advanced capabilities for materials modelling with QUANTUM ESPRESSO, J. Phys.: Condens. Matter. 29 (2017) 465901, http://dx.doi.org/10.1088/1361-648X/aa8f79.

[21] J.P. Perdew, K. Burke, M. Ernzerhof, Generalized gradient approximation made simple, Phys. Rev. Lett. 77 (18) (1996) 3865–3868, http://dx.doi.org/10.1103/PhysRevLett.77.3865.

[22] P.E. Blöchl, Projector augmented-wave method, Phys. Rev. B 50 (24) (1994) 17953–17979, http://dx.doi.org/10.1103/PhysRevB.50.17953.

[23] A. Dal Corso, Pseudopotentials periodic table: From H to Pu, Comput. Mater. Sci. 95 (2014) 337–350, http://dx.doi.org/10.1016/j.commatsci.2014.07.043.

[24] PAW pseudopotentials for the Ru, O and H atoms were taken from the Quantum ESPRESSO Pseudopotential Library (files: `Ru.pbe-spn-kjpaw_psl.1.0.0.UPF`, `O.pbe-n-kjpaw_psl.1.0.0.UPF`, `H.pbe-kjpaw_psl.1.0.0.UPF`), 2024, http://pseudopotentials.quantum-espresso.org/legacy_tables.

[25] H.J. Monkhorst, J.D. Pack, Special points for Brillouin-zone integrations, Phys. Rev. B 13 (12) (1976) 5188–5192, http://dx.doi.org/10.1103/PhysRevB.13.5188.

[26] M. Methfessel, A.T. Paxton, High-precision sampling for Brillouin-zone integration in metals, Phys. Rev. B 40 (6) (1989) 3616–3621, http://dx.doi.org/10.1103/PhysRevB.40.3616.

[27] S. Grimme, J. Antony, S. Ehrlich, H. Krieg, A consistent and accurate ab initio parametrization of density functional dispersion correction (DFT-D) for the 94 elements H-Pu, J. Chem. Phys. 132 (15) (2010) 154104, http://dx.doi.org/10.1063/1.3382344.

[28] L. Bengtsson, Dipole correction for surface supercell calculations, Phys. Rev. B 59 (19) (1999) 12301–12304, http://dx.doi.org/10.1103/PhysRevB.59.12301.

[29] H. Ogasawara, B. Brena, D. Nordlund, M. Nyberg, A. Pelmenschikov, L.G.M. Pettersson, A. Nilsson, Structure and bonding of water on Pt(111), Phys. Rev. Lett. 89 (27) (2002) 276102, http://dx.doi.org/10.1103/PhysRevLett.89.276102.

[30] O. Andreussi, I. Dabo, N. Marzari, Revised self-consistent continuum solvation in electronic-structure calculations, J. Chem. Phys. 136 (6) (2012) 064102, http://dx.doi.org/10.1063/1.3676407.

[31] G. Henkelman, H. Jónsson, Improved tangent estimate in the nudged elastic band method for finding minimum energy paths and saddle points, J. Chem. Phys. 113 (22) (2000) 9978–9985, http://dx.doi.org/10.1063/1.1323224.

[32] G. Henkelman, B.P. Uberuaga, H. Jónsson, A climbing image nudged elastic band method for finding saddle points and minimum energy paths, J. Chem. Phys. 113 (22) (2000) 9901–9904, http://dx.doi.org/10.1063/1.1329672.

[33] G.T. Barkema, N. Mousseau, Event-based relaxation of continuous disordered systems, Phys. Rev. Lett. 77 (21) (1996) 4358–4361, http://dx.doi.org/10.1103/PhysRevLett.77.4358.

[34] M. Poberznik, M. Gunde, N. Salles, A. Jay, A. Hemeryck, N. Richard, N. Mousseau, L. Martin-Samos, pARTn: A plugin implementation of the activation relaxation technique nouveau that takes over the FIRE minimisation algorithm, Comput. Phys. Comm. 295 (2024) 108961, http://dx.doi.org/10.1016/j.cpc.2023.108961.

[35] R.F. Ribeiro, A.V. Marenich, C.J. Cramer, D.G. Truhlar, Use of solution-phase vibrational frequencies in continuum models for the free energy of solvation, J. Phys. Chem. B 115 (49) (2011) 14556–14562, http://dx.doi.org/10.1021/jp205508z.

[36] M. Poberžnik, D. Costa, A. Hemeryck, A. Kokalj, Insight into the bonding of silanols to oxidized aluminum surfaces, J. Phys. Chem. C 122 (17) (2018) 9417–9431, http://dx.doi.org/10.1021/acs.jpcc.7b12552.

[37] S. Maintz, V.L. Deringer, A.L. Tchougréeff, R. Dronskowski, LOBSTER: A tool to extract chemical bonding from plane-wave based DFT, J. Comput. Chem. 37 (11) (2016) 1030–1035, http://dx.doi.org/10.1002/jcc.24300.

[38] A. Kokalj, XCrySDen—a new program for displaying crystalline structures and electron densities, J. Mol. Graph. Model. 17 (1999) 176–179, http://dx.doi.org/10.1016/S1093-3263(99)00028-5, code available from http://www.xcrysden.org/.

[39] T. Williams, C. Kelley, et al., Gnuplot 6.0, 2023, http://www.gnuplot.info/.

[40] Inkscape Project, Inkscape, version 1.4, 2025, https://inkscape.org.

[41] C. Cai, K. Liu, Y. Zhu, P. Li, Q. Wang, B. Liu, S. Chen, H. Li, L. Zhu, H. Li, J. Fu, Y. Chen, E. Pensa, J. Hu, Y.-R. Lu, T.-S. Chan, E. Cortés, M. Liu, Optimizing hydrogen binding on Ru sites with RuCo alloy nanosheets for efficient alkaline hydrogen evolution, Angew. Chem. 134 (4) (2022) e202113664, http://dx.doi.org/10.1002/ange.202113664.

[42] M. Smiljanić, S. Panić, M. Bele, F. Ruiz-Zepeda, L. Pavko, L. Gašparič, A. Kokalj, M. Gaberšček, N. Hodnik, Improving the HER activity and stability of Pt nanoparticles by titanium oxynitride support, ACS Catal. 12 (20) (2022) 13021–13033, http://dx.doi.org/10.1021/acscatal.2c03214.